Check for updates

ADVANCED ENERGY MATERIALS
www.advenergymat.de

Unlocking Electrode Performance of Disordered Rocksalt Oxides Through Structural Defect Engineering and Surface Stabilization with Concentrated Electrolyte

*Yanjia Zhang, Yosuke Ugata, BenoîtDenis Louis Campéon, and Naoaki Yabuuchi**

Li-excess cation-disordered rocksalt oxides can boost the energy density of rechargeable batteries by using anionic redox, but the inferior reversibility of anionic redox hinders its use for practical applications. Herein, a binary system of Li_3NbO_4–$LiMnO_2$ is targeted and the systematic study on factors affecting electrode reversibility, *i.e.*, percolation probability, electronic conductivity, defect concentrations, and electrolyte solutions, is conducted. A Mn-rich sample, $Li_{1.1}Nb_{0.1}Mn_{0.8}O_2$, delivers a smaller reversible capacity compared with a Li-rich sample, $Li_{1.3}Nb_{0.3}Mn_{0.4}O_2$, because of the limitation of ionic migration associated with insufficient percolation probability for disordered oxides. Nevertheless, a larger reversible capacity of $Li_{1.3}Nb_{0.3}Mn_{0.4}O_2$ originates from excessive activation of anionic redox, leading to the degradation of electrode reversibility. The superior performance of $Li_{1.1}Nb_{0.1}Mn_{0.8}O_2$, including Li ion migration kinetics and electronic transport properties, is unlocked by the enrichment of structural defects for nanosized oxides. Moreover, electrode reversibility is further improved by using a highly concentrated electrolyte solution with $LiN(SO_2F)_2$ through the surface stabilization on high-voltage exposure. Superior capacity retention, >100 cycles, is achieved for nanosized $Li_{1.1}Nb_{0.1}Mn_{0.8}O_2$. The electrolyte decomposition and surface stabilization mechanisms are also carefully examined, and it is revealed that the use of highly concentrated electrolyte solution can effectively prevent lattice oxygen being further oxidized and transition metal ion dissolution.

1. Introduction

Since its first commercialization of $LiCoO_2$, the rechargeable Li-ion batteries (LIBs) have become the dominant energy storage technology in various applications.[1] To meet the growing demand for large-scale applications of LIBs, further improvement of energy density of state-of-the-art LIB is indispensable.[2,3] Energy density of LIBs is generally restricted by positive electrode materials. Over the past two decades, stoichiometric layered-type lithium transition metal (TM) oxides, denoted as $LiMO_2$, have been extensively developed.[4–6] However, those theoretical capacities as electrode materials are restricted by the limited amount of Li ions in host structures. Layered-type Li-rich metal oxides, $Li_{1+x}M_{1-x}O_2$ with excess Li ions, which are substituted for transition metal ions, can boost the reversible capacity to 250 – 280 mA h g^{-1} through the activation of anionic redox reaction of oxide ions (O^{2-}/O^{n-}).[7,8] Nonetheless, the oxidation of anionic host structures in the Li-excess layered structure is accompanied by irreversible TM ions migration, resulting in a pronounced irreversible structural evolution, including oxygen loss, leading to voltage decay on electrochemical cycles.[9,10]

Rocksalt-type metal oxides are promising positive electrode materials thanks to their robust 3D host structures based on cation disordered arrangement. Indeed, compared to traditional layered materials, Li-rich metal oxides with the cation-disordered rocksalt (DRS) structure exhibit superior structural stability using highly reversible multi-electron cationic redox, Mn^{2+}/Mn^{4+},[11] Mo^{3+}/Mo^{6+},[12] V^{3+}/V^{5+},[13] *etc.*[14] Note that TM migration also occurrs in Mo/V-based DRS oxides, but this process is highly reversible without capacity loss. Very recently, almost no volume changes with excellent cyclability have been confirmed in $Li_{8/7}V_{4/7}Ti_{2/7}O_2$, which is found in a binary solid solution system between Li_2TiO_3 and $LiVO_2$, and this unique character is achieved by two-electron V cationic redox coupled with migration of V ions.[15] Although DRS oxides have structural advantage, the electrode performance is suffered from the inferior electrode kinetics. The degradation of electrode reversibility is

Y. Zhang, Y. Ugata, B. L. Campéon, N. Yabuuchi
Advanced Chemical Energy Research Center, Institute of Advanced Sciences
Yokohama National University
Yokohama, Kanagawa 240–8501, Japan
E-mail: yabuuchi-naoaki-pw@ynu.ac.jp

Y. Ugata, N. Yabuuchi
Department of Chemistry and Life Science
Yokohama National University
Yokohama, Kanagawa 240–8501, Japan

B. L. Campéon
University Grenoble Alpes
University Savoie Mont Blanc
CNRS, Grenoble INP, LEPMI, Grenoble 38402, France

The ORCID identification number(s) for the author(s) of this article can be found under https://doi.org/10.1002/aenm.202304074

© 2024 The Authors. Advanced Energy Materials published by Wiley-VCH GmbH. This is an open access article under the terms of the Creative Commons Attribution License, which permits use, distribution and reproduction in any medium, provided the original work is properly cited.

DOI: 10.1002/aenm.202304074

also inevitable when the anionic redox is activated. Percolative Li ion migration pathway of Li-excess DRS oxides results in relatively larger activation barriers for Li ion migration, and thus inferior electrode kinetics, compared to layered oxides, restricting rate capability as electrode materials.[16] This phenomenon is particularly pronounced in samples with micrometer-sized particles,[17,18] nano-sized particles has much better kinetics that facilities high rate performance.[19] Moreover, the addition of Nb^{5+}/Ti^{4+} with insulating character led to less probability for the formation of electronic percolative network consisting of conductive TM ions, by which electronic conductivity is considered to be reduced. Therefore, reduction of particle size and enrichment of structural defects are necessary to facilitate Li ion migration and electronic conduction. Noticeably, higher energy density as electrode materials coupled with the activation of anionic redox is boosted to ≈1000 Wh kg^{-1}, especially for Li-rich Mn-based oxides and oxyfluorides.[11,18]

Although higher energy density, which originates from the activation of anionic redox, is obtained for Li-rich Mn-based oxides/oxyfluorides, an unanswered practical issue is found in insufficient reversibility of anionic redox. The unstable/irreversible anionic redox easily triggers oxygen loss after charge to higher voltage, leading to insufficient cycle stability. Therefore, further stabilization of anionic redox is essential for the use of practical applications.[20,21] Stabilization mechanisms of anionic redox for DRS oxides with different TMs have been reported in literature, for instance, the stabilization of oxidized oxygen through π-type interaction with t_{2g} orbitals of Mn ions[22,23], σ-type interaction with e_g orbitals of Ni ions,[24] and both π-type and σ-type interaction with Co ions with the intermediate spin state.[25] Nevertheless, the excessive use of anionic redox inevitably leads to oxygen loss due to the intrinsic chemical instability of anionic species after charge to high voltage. Although the anionic redox reversibility is partially improved through π-type interaction, the activation of anionic redox results in the interaction of neighboring oxidized oxygen species, leading to oxygen dimerization. One strategy for the anionic redox stabilization is the use of highly covalent bonds through Li_3PO_4 integration with P^{5+} ions located at tetrahedral sites. The presence of P ions coupled with the suppression of oxygen dimerization improves electrode reversibility[26] and thermal stability.[27] Another strategy is fluorination process (Li-rich oxyfluorides), and fluorination decreases average oxidation states of transition metal ions due to the decreased anionic charge, and thus cationic redox capacity is increased, especially for low-valence redox-active TMs, for instance, $Li_2Mn^{2+}{}_{2/3}Nb_{1/3}O_2F$[11] and $Li_2Mn^{2+}{}_{1/2}Mn^{3+}{}_{1/2}O_{1.5}F_{1.5}$.[28] Moreover, it is proved that fluorination favors creating Li-rich clusters that facilitate Li ion percolative conduction[29] and the addition of F ions suppresses the partial structural transition to spinel phase during cycling.[30] Nevertheless, Li_3PO_4 integrated DRS and Li-rich oxyfluorides are metastable phases synthesized by high-energy mechanical milling, which limits its use for practical applications.

An emerging new approach to improve the anionic redox reversibility is the use of highly concentrated electrolyte (HCE) solutions. For HCEs, nearly all solvents are coordinated to Li ions, and therefore better oxidation stability as electrolyte is achieved.[31] Higher salt concentrations result in higher viscosity of electrolyte, and therefore a conventional polyolefin separator cannot be used for HCEs. Recently, this practical problem is effectively solved by coating of a meta-aramid resin on the polyolefin separator.[32] Indeed, the reversibility of anionic redox is significantly improved by using HCE with the meta-aramid coated separator, but detailed improved mechanisms are still unclear.[32] Therefore, further studies on DRS oxides with anionic redox combined with HCEs, especially for interfacial stabilization mechanisms, are necessary.

In this work, factors affecting electrode performance in x Li_3NbO_4 – (1–x) $LiMnO_2$ binary system mainly with earth abundant Mn ions are systematically examined. After careful experimental design, advanced DRS oxides with improved electrode kinetics and electrode reversibility, >100 cycles, with a higher discharge capacity (200 Ma h g^{-1}) are successfully attained. Less Li-excess and Mn-rich $Li_{1.1}Nb_{0.1}Mn_{0.8}O_2$ positive electrode exhibits better capacity retention and good electronic conductivity compared to $Li_{1.3}Nb_{0.3}Mn_{0.4}O_2$. Nonetheless, the reversible capacity of micrometer-sized $Li_{1.1}Nb_{0.1}Mn_{0.8}O_2$ is limited by the sluggish Li ion migration kinetics associated with the insufficient connection for percolative Li conduction paths. These problems are well addressed through mechanical milling and defect engineering, and nanosized $Li_{1.1}Nb_{0.1}Mn_{0.8}O_2$ with enriched structural defects shows significantly improved electrode kinetics with further higher electronic conductivity. Nevertheless, defect engineering on $Li_{1.1}Nb_{0.1}Mn_{0.8}O_2$ increases instability of oxide surface on charge. This unfavorable side effect is also effectively mitigated by the use of HCE (5.5 M $LiN(SO_2F)_2$, LiFSA, in dimethyl carbonate, DMC), and the suppression of electrolyte decomposition and Mn ion dissolution is clearly evidenced. These combined strategies unlock the electrode performance of Li-excess DRS electrodes with Mn ions which is suitable for practical battery applications.

2. Results and Discussion

2.1. Optimization of Cationic/Anionic Redox and Short-Range Cation Ordering

For Mn-based Li-excess DRS oxides, the anionic redox contribution on reversible capacities significantly influences electrode reversibility.[33] As shown in Figure S1 (Supporting Information), an increase in the Li_3NbO_4 fraction for Li_3NbO_4–$LiMnO_2$ binary system leads to larger theoretical capacities using anionic redox. Herein, the optimal fraction of Li_3NbO_4 in this binary system is explored. As shown in **Figure 1a**, the crystal structures of the samples were analyzed by X-ray diffraction (XRD). After the calcination, there are no residual phases corresponding to Li_3NbO_4 and $LiMnO_2$, indicating a cation DRS phase is obtained for $Li_{1.3}Nb_{0.3}Mn_{0.4}O_2$, $Li_{1.2}Nb_{0.2}Mn_{0.6}O_2$, and $Li_{1.1}Nb_{0.1}Mn_{0.8}O_2$ with a space group symmetry of *Fm*-3*m* in which all cations are located at 4*a* sites. In addition, $Li_{1.1}Nb_{0.1}Mn_{0.8}O_2$ is synthesized as the maximum Mn content in Li_3NbO_4–$LiMnO_2$ binary system (Figure S2, Supporting Information), and it is also concluded that the particle size is significantly influenced by the heating time. A smaller particle size sample with large surface area is obtained by shorter heating time at 1050 °C. Note that further enrichment of Mn ions is unsuccessful, and the presence of Mn-rich phase is observed. Nb^{5+} (0.64 Å) ions have a similar ionic radius with Mn^{3+} ion (0.645 Å in a high-spin configuration), but Li^+ ion (0.76 Å) is clearly larger compared with both transition metal

© 2024 The Authors. Advanced Energy Materials published by Wiley-VCH GmbH

16146840, 2024, 23, Downloaded from https://onlinelibrary.wiley.com/doi/10.1002/aenm.202304074 by Yokohama National University, Wiley Online Library on [09/10/2024]. See the Terms and Conditions (https://onlinelibrary.wiley.com/terms-and-conditions) on Wiley Online Library for rules of use; OA articles are governed by the applicable Creative Commons License

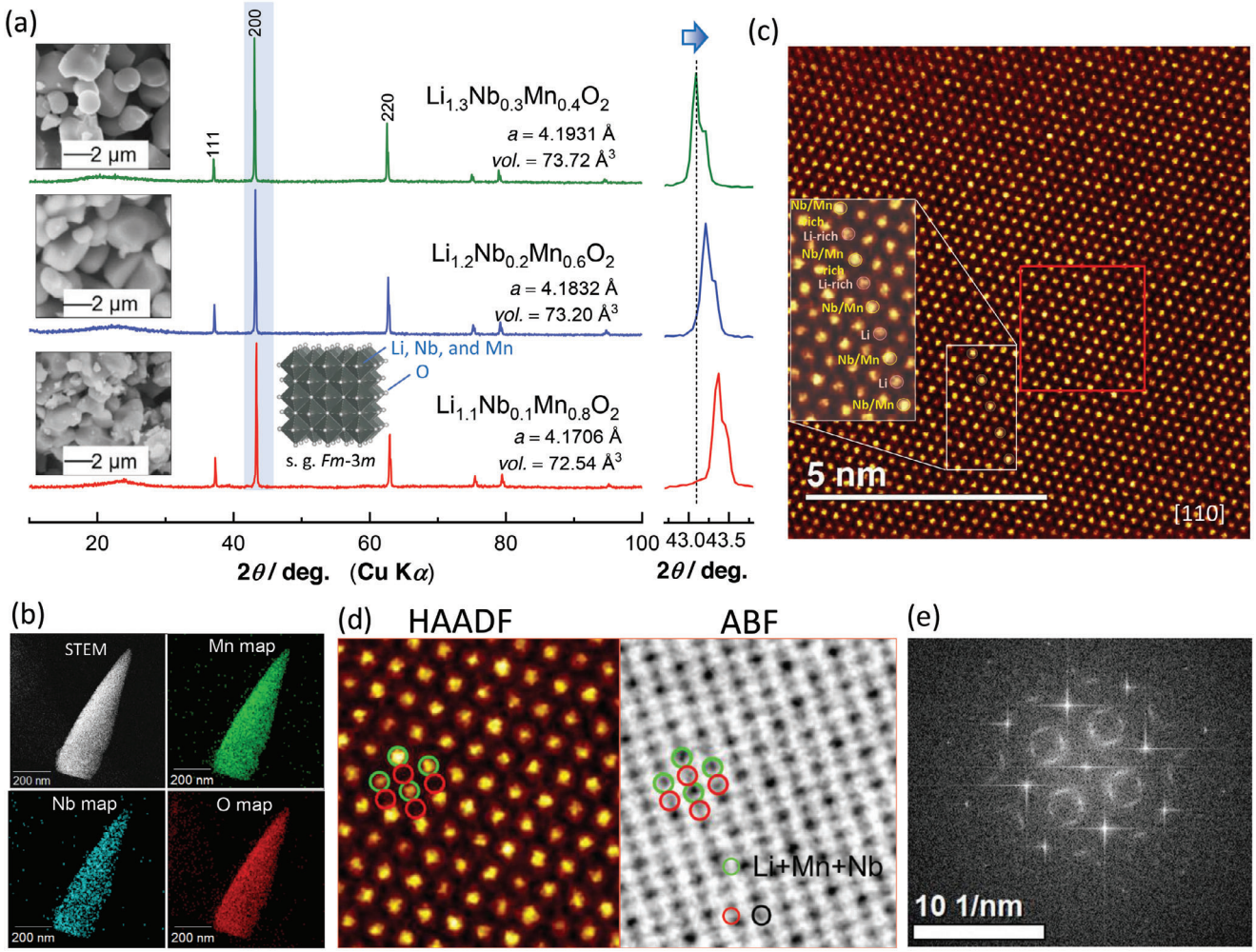

Figure 1. Structural characterization: a) XRD patterns and SEM images of as-prepared $Li_{1.3}Nb_{0.3}Mn_{0.4}O_2$, $Li_{1.2}Nb_{0.2}Mn_{0.6}O_2$, and $Li_{1.1}Nb_{0.1}Mn_{0.8}O_2$ and a schematic illustration of DRS structure drawn using the program VESTA,[59] b) STEM/EDX images of $Li_{1.1}Nb_{0.1}Mn_{0.8}O_2$, c) HAADF-STEM image of $Li_{1.1}Nb_{0.1}Mn_{0.8}O_2$, d) HAADF/ABF-STEM images of magnified region of (c), where a short-range cation disordered arrangement for cations is noted along [011], and e) FFT image of STEM image along [001] (original STEM images are shown in Figure S5, Supporting Information).

ions. Therefore, the reduction of Li_3NbO_4 fraction leads to a smaller lattice parameter, which can be evidenced by the peak shift in the diffraction lines to the higher angle. The lattice parameter of 4.193 Å for $Li_{1.3}Nb_{0.3}Mn_{0.4}O_2$ is decreased to 4.171 Å for $Li_{1.1}Nb_{0.1}Mn_{0.8}O_2$. The reduction of Li_3NbO_4 fraction, in which both cations have an insulating character, is supposed to favorable for electron conduction, but the probability of percolative connection for Li ions migration paths is decreased. All these three samples show similar particle morphology and sizes, and uniform distribution of Nb, Mn, and O ions (Figure 1b; Figure S3, Supporting Information). To further characterize the crystal structure of $Li_{1.1}Nb_{0.1}Mn_{0.8}O_2$, annular bright field (ABF) and high-angle annular dark field (HAADF) STEM characterizations were conducted and summarized in Figure 1c, d and Figures S4 and S5 (Supporting Information). Although a uniform contrast for anionic sites (O ions) from an ABF-STEM image, in which the presence of lighter atoms is emphasized, is observed (Figure 1d), a non-uniform contrast is found for the cationic sites, which is clearly evidenced in an HAADF image, in which heavier transition metal ions are clearly visualized. This observation, non-uniform contrast only for the cationic sites, suggests that the presence of short-range ordering (SRO) for Li/Mn/Nb ions, and the bright contrast site in the HADDF image indicates Mn/Nb rich sites, and the darker contrast site indicates Li rich sites (Figure 1c). Similar short-range ordering is observed for $Li_{1.2}Mn_{0.4}Zr_{0.4}O_2$, but less ordering is observed for $Li_{1.2}Mn_{0.4}Ti_{0.4}O_2$.[34] The cation-short range ordering is also evidenced from the diffuse spots in the FFT image obtained from the STEM image (Figure 1e). The presence of SRO would influence Li transport properties by modifying both local and macroscopic environments related to percolative Li ions conduction,[20,34] which is further discussed in the later section.

To further study the impact of chemical compositions on electrode performance, galvanostatic charge/discharge curves of $Li_{1.3}Nb_{0.3}Mn_{0.4}O_2$, $Li_{1.2}Nb_{0.2}Mn_{0.6}O_2$, and $Li_{1.1}Nb_{0.1}Mn_{0.8}O_2$ at a rate of 10 mA g^{-1} between 1.5 and 4.8 V are compared in **Figure 2a**. Theoretical capacities of these compounds based on Li contents are calculated to be ≈384, 350, and 317 mA h g^{-1}

© 2024 The Authors. Advanced Energy Materials published by Wiley-VCH GmbH

16146840, 2024, 23, Downloaded from https://onlinelibrary.wiley.com/doi/10.1002/aenm.202304074 by Yokohama National University, Wiley Online Library on [09/10/2024]. See the Terms and Conditions (https://onlinelibrary.wiley.com/terms-and-conditions) on Wiley Online Library for rules of use; OA articles are governed by the applicable Creative Commons License

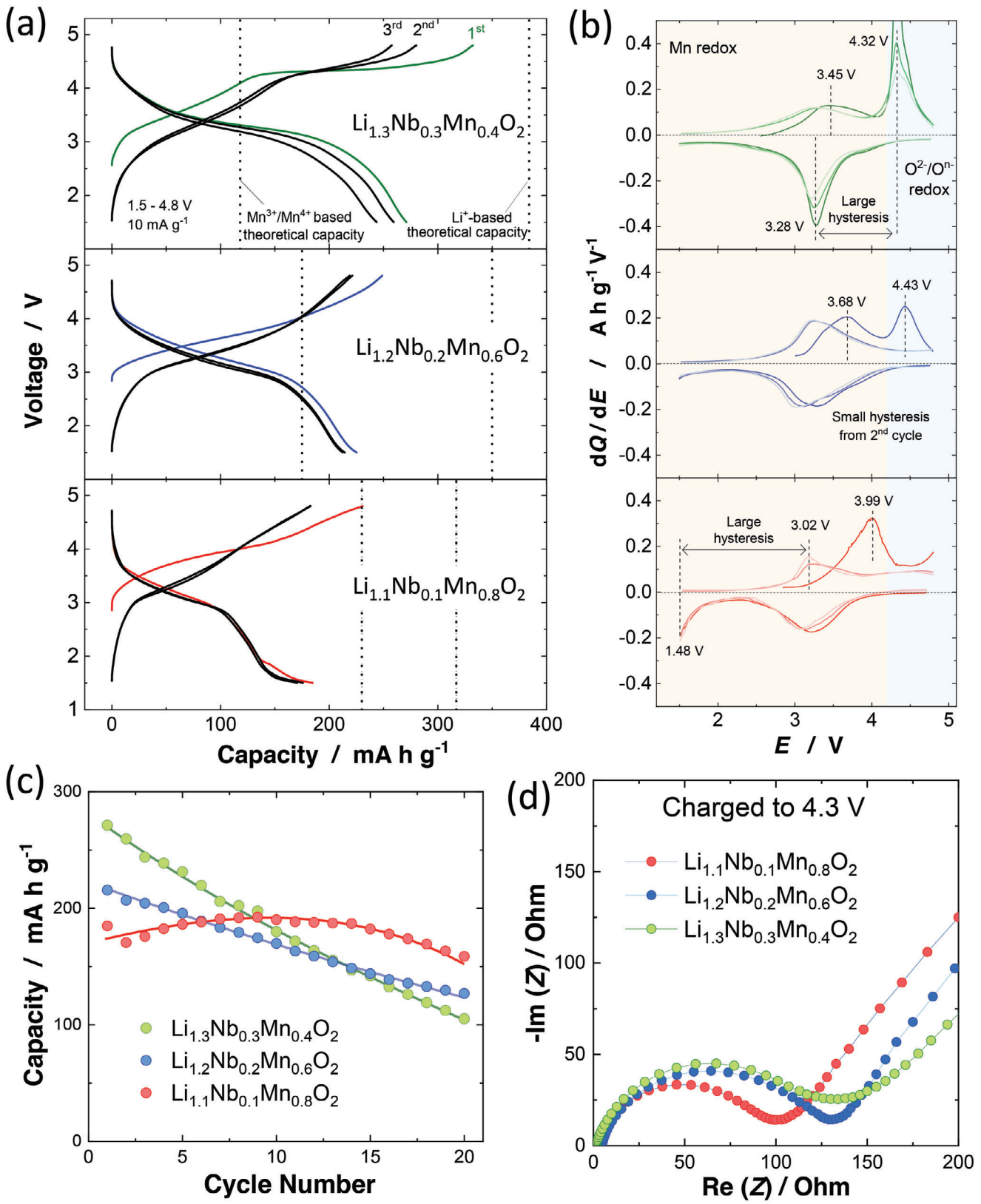

Figure 2. Electrode performance of $Li_{1.3}Nb_{0.3}Mn_{0.4}O_2$, $Li_{1.2}Nb_{0.2}Mn_{0.6}O_2$, and $Li_{1.1}Nb_{0.1}Mn_{0.8}O_2$: a) Galvanostatic charge/discharge curves in Li cells, b) corresponding differential capacity curves as a function of voltage, c) capacity retention, and d) EIS data after charged to 4.3 V.

© 2024 The Authors. Advanced Energy Materials published by Wiley-VCH GmbH

16146840, 2024, 23, Downloaded from https://onlinelibrary.wiley.com/doi/10.1002/aenm.202304074 by Yokohama National University, Wiley Online Library on [09/10/2024]. See the Terms and Conditions (https://onlinelibrary.wiley.com/terms-and-conditions) on Wiley Online Library for rules of use; OA articles are governed by the applicable Creative Commons License

for $Li_{1.3}Nb_{0.3}Mn_{0.4}O_2$, $Li_{1.2}Nb_{0.2}Mn_{0.6}O_2$, and $Li_{1.1}Nb_{0.1}Mn_{0.8}O_2$, and 118, 175, and 230 mA h g^{-1} based on Mn^{3+}/Mn^{4+} redox, respectively. A clear difference in the electrochemical behavior is observed among the three samples due to the difference in the dominant redox species. $Li_{1.3}Nb_{0.3}Mn_{0.4}O_2$ electrode has the lowest Mn redox capacity contribution, which can be obtained from the slope region of the first charging. A large charge capacity (≈300 mA h g^{-1}) is observed based on a larger contribution of anionic redox, which is clearly evidenced from a long voltage plateau at 4.3 V.[18] Note that the voltage plateau is clearly observed at the second cycle, and a large voltage hysteresis on charge/discharge is evidenced. Such hysteresis is also observed for a layered system,[35] which would originate from irreversible oxygen dimerization. Nevertheless, the anionic redox plateau for $Li_{1.3}Nb_{0.3}Mn_{0.4}O_2$ is gradually disappeared, indicating the inferior reversibility for anionic redox. The oxygen redox plateau is less visible for a less Li-excess system, $Li_{1.2}Nb_{0.2}Mn_{0.6}O_2$, and no clear evidence of anionic redox is observed from the second cycle. Moreover, the voltage hysteresis is less pronounced, suggesting that reversible capacities mainly originate from Mn cationic redox with a small contribution of anionic redox.

When the Li amount is further decreased, the electrode reversibility is significantly deteriorated. For $Li_{1.1}Nb_{0.1}Mn_{0.8}O_2$ with the maximum Mn content, discharge voltage profiles are clearly changed, and an additional voltage plateau at 1.5 V on discharge appears. A large voltage hysteresis is also noted for Mn^{3+}/Mn^{4+} cationic redox (Figure 2b). This fact clearly indicates that the penalty for Li percolative Li conduction cannot be avoided for the less Li composition DRS oxide. Nevertheless, as shown in Figure 2c, $Li_{1.1}Nb_{0.1}Mn_{0.8}O_2$ shows the best cyclability, and the capacity retention reaches 87% after 20 cycles. Note that the capacity is gradually increased in the initial few cycles because of the phase transition from pure cation disordered rocksalt phase to partial spinel-like ordering,[36] and such a phase transition for the Mn^{3+}-rich sample can be suppressed in nano-sized cation disordered rocksalt oxide materials.[37] In contrast, $Li_{1.3}Nb_{0.3}Mn_{0.4}O_2$ shows the retention of 31% at the same condition. A similar trend is also obtained for cycling with a voltage range of 2.0–4.8 V (Figure S6, Supporting Information). Another important factor is the enrichment of Mn ions, which is electronic conductive species. Electrochemical impedance spectroscopy (EIS) measurements (Figure 2d) confirm the increased amount of Mn ions results in a smaller semicircle, which reflects Li ion/electron conduction in the composite electrode, coupled with charge transfer resistance.[38] The observed differences from these three oxides with different Li/Mn contents suggest that electrode performance, related to cationic/anionic redox, is systematically tuned by the optimization of chemical compositions.

2.2. Improved Electrode Kinetics through Crystalline Size Reduction and Defect Engineering

Although good cyclability is realized for micrometer-sized $Li_{1.1}Nb_{0.1}Mn_{0.8}O_2$, the reversible capacity is relatively small, 150 mA h g^{-1} at a rate of 10 mA g^{-1} in a range of 1.5–4.8 V, which originates from the penalty of Li ion percolative conduction in the DRS oxide. To further improve electrode reversibility, Li ion migration kinetics and electronic conductivity need to be enhanced. To mitigate the penalty of Li ion percolative conduction, the decrease in Li ion migration path length is necessary. Therefore, the mechanical milling was conducted at 450 rpm with different duration, 3, 6, and 12 h (Figure S7, Supporting Information), to optimize crystalline sizes. **Figure 3a** compares synchrotron XRD (SXRD) patterns of the samples with different milling duration. Although the DRS structure is retained after milling, broader diffraction profiles are observed after mechanical milling, indicative of the reduction of crystallinity as a function of milling time. Although a significant change is noted for morphology observed in a SEM image, a crystallinity change is relatively small from an SXRD pattern after 3 h mechanical milling (denoted as "450 rpm 3 h"). After further extension of the milling time to 6 h (450 rpm 6 h) and 12 h (450 rpm 12 h), a clear reduction of crystallinity with wider peak widths is noted from SXRD patterns for both samples. However, the mechanical milling after 12 h leads to the agglomeration of secondary particles, and this fact may originate from the excess enrichment of strains and defects to the sample by high-energy mechanical milling. Furthermore, to improve the electrode reversibility, nanosized $Li_{1.1}Nb_{0.1}Mn_{0.8}O_2$ samples were further mixed with acetylene black (AB), and XRD and SEM studies reveal that nanosized oxides with the uniform particle size are obtained after milling at 450 rpm for 6 h (Figure S8, Supporting Information).

DF-STEM and BF-STEM images with different magnifications of $Li_{1.1}Nb_{0.1}Mn_{0.8}O_2$, as-prepared and mechanical milled samples for 6 h, are compared in Figure 3b and Figure S9 (Supporting Information). Both particle size and crystalline size are clearly reduced by mechanical milling, and a significant reduction of particle size, compared with as-prepared (500 nm), and nanosized grains (≈150 nm) consisting of nanosized crystalline particles (< 10 nm) are observed. Similar characters with agglomerated nanosized crystalline particles are generally observed for the sample synthesized by high-energy mechanical milling.[17,39] Moreover, for nanosized $Li_{1.1}Nb_{0.1}Mn_{0.8}O_2$, the short-range cation ordering observed for the as-prepared sample is not evidenced from a FFT image obtained from a high-resolution STEM image. Raman spectroscopy has been conducted to study the defect engineering (Figure S10, Supporting Information). The main peak at 602 cm^{-1} for the as-prepared sample is assigned as the vibration of the Mn—O bonds, this peak is gradually changed to higher wavenumbers after milling at 450 rpm for 3, 6, and 12 h, suggesting the enrichment of defect concentration as milling time increases.[40] The relationship between crystallite sizes and strains of the samples was further analyzed by Williamson–Hall method,[41] the Williamson–Hall equation is simply expressed as follow:[42]

$$\beta \cos\theta = \frac{K\lambda}{t} + 4\varepsilon \sin\theta \quad (1)$$

where β is the integrated width of each peak, K is the shape factor (≈0.9), θ is the peak position, ε is the integral breadth from strain, λ is the wavelength of X-ray, and t is the apparent crystallite size. A CeO_2 standard is used to determine the instrumental broadening. As shown in Figure S11 (Supporting Information), the apparent crystallite size of CeO_2 standard is 97 nm with different d-spacing, indicating the instrumental broadening and strain are negligible.[43] A similar result can be found from the

© 2024 The Authors. Advanced Energy Materials published by Wiley-VCH GmbH

16146840, 2024, 23, Downloaded from https://onlinelibrary.wiley.com/doi/10.1002/aenm.202304074 by Yokohama National University, Wiley Online Library on [09/10/2024]. See the Terms and Conditions (https://onlinelibrary.wiley.com/terms-and-conditions) on Wiley Online Library for rules of use; OA articles are governed by the applicable Creative Commons License

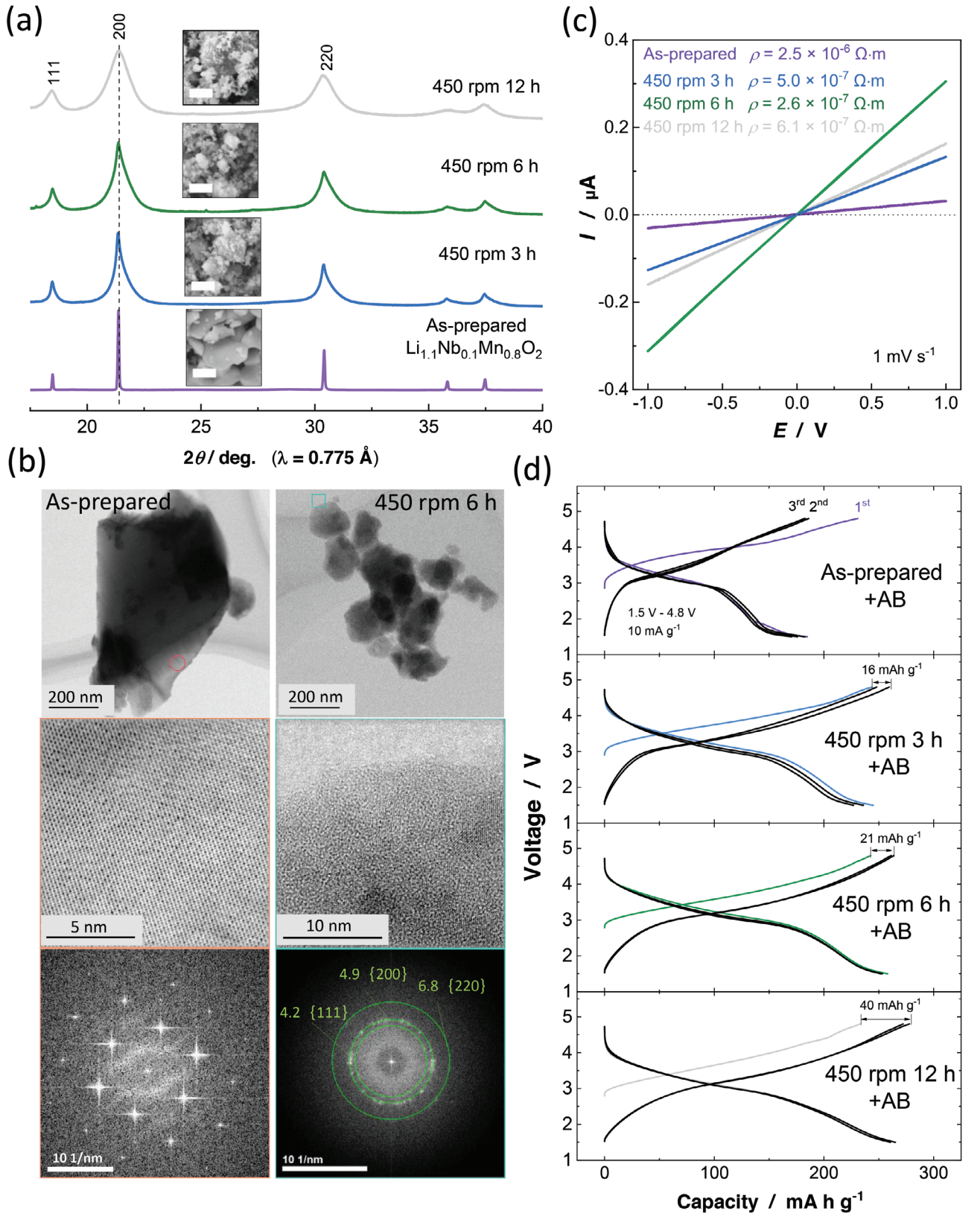

Figure 3. a) SXRD patterns and SEM images of as-prepared and mechanical milled samples (scale bar, 2 μm), b) STEM and FFT images of as-prepared and 6 h milled $Li_{1.1}Nb_{0.1}Mn_{0.8}O_2$, c) CV curves of $Li_{1.1}Nb_{0.1}Mn_{0.8}O_2$ powders in different mechanical milling conditions at scan rate of 1 mV s^{-1}, and d) comparison of electrochemical properties of $Li_{1.1}Nb_{0.1}Mn_{0.8}O_2$ with different milling duration.

© 2024 The Authors. Advanced Energy Materials published by Wiley-VCH GmbH

16146840, 2024, 23, Downloaded from https://onlinelibrary.wiley.com/doi/10.1002/aenm.202304074 by Yokohama National University, Wiley Online Library on [09/10/2024]. See the Terms and Conditions (https://onlinelibrary.wiley.com/terms-and-conditions) on Wiley Online Library for rules of use; OA articles are governed by the applicable Creative Commons License

as-prepared sample with nearly no crystal imperfections. However, after ball-milling process, the slope ϵ changed from 2.40×10^{-3} (as-prepared) to 2.32×10^{-2} (450 rpm 3 h), 3.63×10^{-2} (450 rpm 6 h), and 3.98×10^{-2} (450 rpm 12 h), suggesting the increase of strain by ball milling. The lattice strain is increased with increasing milling time up to 6 h, and further ball-milling has less impact on the strain and leads to particle agglomeration. For nanosized samples, many structural defects are expected to be present as shown in Figure 3a,b, but the influence of these defects on electronic conductivity of the samples, is not fully understand. Therefore, the electronic conductivity of the samples was briefly measured for compressed powders, and an experimental setup is described in Figure S12a (Supporting Information). The resistivity ρ is calculated based on the following formula: $\rho = RS/L$, where R is a resistance for electron conduction calculated from a slope of a cyclic voltammogram, S is the area of compressed powder, and L is compressed powder thickness. Note that the density of compressed powder pellets is not high enough compared with sintered and dense pellets, the resistivity of the samples obtained by this methodology is expected to be smaller compared with dense pellets. Nevertheless, a trend of resistivity changes for samples by different mechanical milling duration, and thus the impact of defects on sample resistivity, can be discussed. As shown in Figure 3c, the slopes of cyclic voltammograms are increased with increasing the milling time to 6 h. Current flow is 20 times larger for the sample milled for 6 h compared with the as-prepared sample, indicating that nanosized samples show much better electronic conductivity. Note that these data are successfully reproduced from different measurements as shown in Figure S12b (Supporting Information). Mechanical milling reduces the sample particle size, and thus the resistance originating from particle-to-particle interfacial electron conduction is expected to be increased. However, unexpectedly, moderately milled samples show improved electronic conductivity compared with the as-prepared sample, and this fact is proposed to originate from the enrichment of structural defects by milling, which facilitates facile mixed electron/ion conduction. From the comparison between the samples, 6 and 12 h milled samples, excess milling results in inferior electronic conductivity, probably because of excessive enrichment of structural defects, which is further discussed coupled with the electrochemical properties of the samples.

Electrode performances of $Li_{1.1}Nb_{0.1}Mn_{0.8}O_2$ before and after milling are further examined in Li cells, and results are shown in Figure 3d. Mechanically milled samples show larger reversible capacities of 250 – 270 mA h g^{-1} even at room temperature, corresponding to an increase of 100 mA h g^{-1} compared with the micrometer-sized sample. For micrometer-sized $Li_{1.1}Nb_{0.1}Mn_{0.8}O_2$, the lower probability of percolative Li conduction path connection restricts the reversible capacity, and only limited Li sites in the structure are activated. After reducing particle size by milling, the distance of Li migration path is decreased, and the electronic conduction is also improved as shown in Figure 3c and Figure S13, Supporting Information. This experimental finding also suggests that the enrichment of grain boundary concentrations facilitate Li ion migration. Note that the milled sample for 12 h shows faster capacity decay and higher interfacial resistance compared with other tested samples (Figure S13b,c, Supporting Information). Moreover, a smaller initial charge capacity is observed, and this fact indicates that the partial oxidation of the sample by excessive mechanical milling associated with structural defect formation.[15] From these results, it is concluded that the mechanical milling at 450 rpm for 6 h is the best condition to synthesize nanosized sample for $Li_{1.1}Nb_{0.1}Mn_{0.8}O_2$ with good electrode reversibility. The cyclability of nanosized $Li_{1.1}Nb_{0.1}Mn_{0.8}O_2$ is also effectively improved by lowering the upper cut-off charge voltage (Figure S13d, Supporting Information), and 96% of the reversible capacity is retained after 20 cycles at 1.5–4.1 V, mainly with cationic redox. Although the electrode reversibility with higher cut-off charge voltage is still far from the use for practical applications, one promising strategy to improve the reversibility with higher cut-off voltage is surface stabilization, which will be further discussed in the later section.

2.3. Electrode Surface Stabilization using Highly Concentrated Electrolytes

The use of highly concentrated electrolytes (HCEs) has been proposed as an effective strategy to improve the reversibility and cyclability of electrode materials.[31] Herein, the impact of HCE on the electrode performance of nanosized $Li_{1.1}Nb_{0.1}Mn_{0.8}O_2$ is studied in detail. **Figure 4**a,b shows the comparison of the electrode performance of the samples tested with conventional electrolyte (CE, 1 M $LiPF_6$ in EC/DMC) and HCE (5.5 M LiFSA in DMC[44]). Nanosized $Li_{1.1}Nb_{0.1}Mn_{0.8}O_2$ synthesized by mechanical milling at 450 rpm for 6 h was used as the positive electrode material. Nanosized $Li_{1.1}Nb_{0.1}Mn_{0.8}O_2$ with CE delivers a reversible capacity of 220 mA h g^{-1} at a rate of 50 mA g^{-1} (Figure 4a). For nanosized $Li_{1.1}Nb_{0.1}Mn_{0.8}O_2$ with HCE, a reversible capacity is improved by 20 mA h g^{-1}, which is also observed at different current density (Figure S14a,b, Supporting Information). Notably, the cell cycled with CE significantly degrades with cycling at a current rate of 50 mA g^{-1}, and the reversible capacity decreases from 220 to 160 mA h g^{-1} after 40 cycles, corresponding to 73% capacity retention (Figure S14b, Supporting Information). On the contrary, the cell with HCE shows significantly improved capacity retention, and the capacity retention reaches 94% at the same condition. To further study the difference of electrode reactions for both electrolytes, the cells were evaluated by electrochemical impedance spectroscopy (EIS) (Figure 4c,d). EIS measurements were conducted for the cells after 1st and 20th cycles at 4.3 V. Although the cell with HCE shows larger ionic conduction resistance compared with CE, the semicircles in Nyquist plots exhibit smaller size at both 1st and 20th cycles, indicating the electron conduction resistance in the composite electrode and charge transfer resistance for Mn redox coupled with Li ion exchange with electrolyte, are smaller in HCE.[38] These advantages are beneficial to improve the electrode kinetics associated with the suppression of impedance increase on cycles. Indeed, the cell with HCE shows a better rate capability and larger discharge capacity even at 320 mA g^{-1} compared with that with CE (Figure 4e,f). Note that the voltage plateau below 1.8 V is more pronounced at lower current densities, which suggests a slow Li insertion kinetics at the end of discharge. This low voltage plateau is clearly observed for HCE compared with CE, probably due to the faster electrode kinetics in CE with lower viscosity.[45] Extended cycle tests were also performed (Figure 4g), and a better

© 2024 The Authors. Advanced Energy Materials published by Wiley-VCH GmbH

16146840, 2024, 23, Downloaded from https://onlinelibrary.wiley.com/doi/10.1002/aenm.202304074 by Yokohama National University, Wiley Online Library on [09/10/2024]. See the Terms and Conditions (https://onlinelibrary.wiley.com/terms-and-conditions) on Wiley Online Library for rules of use; OA articles are governed by the applicable Creative Commons License

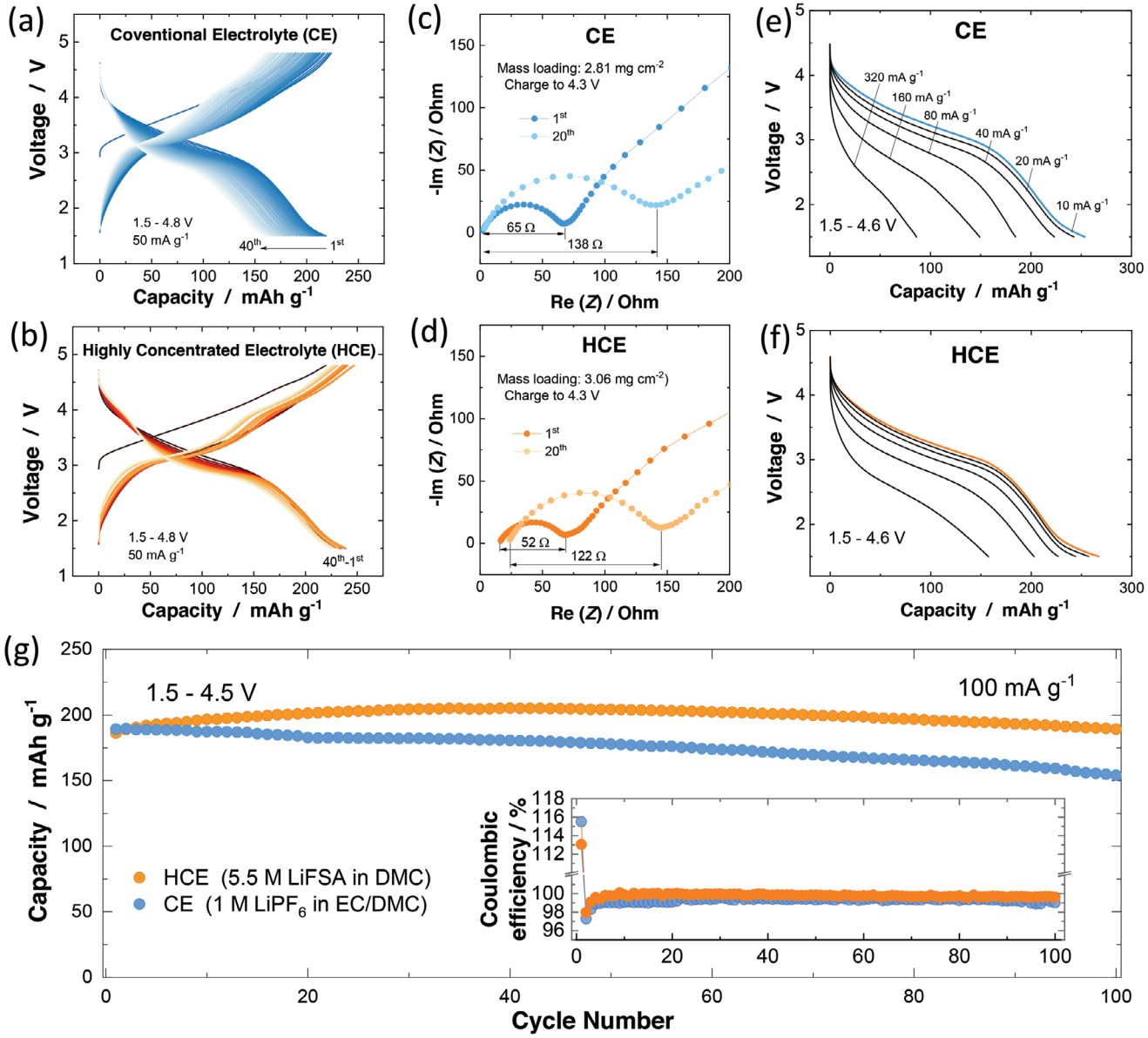

Figure 4. Electrochemical properties of nanosized $Li_{1.1}Nb_{0.1}Mn_{0.8}O_2$, 450 rpm for 6 h, cycled in different electrolyte solutions: a, b) charge/discharge curves, c, d) EIS spectra charged to 4.3 V at 1st and 20th cycle, e, f) rate capability, and g) capacity retention and Coulombic efficiency at a rate of 100 mA g^{-1} for 100 cycle test.

Coulombic efficiency is obtained for HCE due to the reduced side reaction with electrolyte (Figure 4g inset). For 100 continuous cycles, the cell with HCE exhibits superior capacity retention. Moreover, the suppression of voltage profile changes is clearly noted for the cell with HCE (Figure S14c, Supporting Information). Average discharge voltage is gradually reduced for the cell with CE, which is partially mitigated by the use of HCE (Figure S14d, Supporting Information). After 100 cycles, the difference in average discharge voltage reaches 150 mV. Note that, not only for nanosized $Li_{1.1}Nb_{0.1}Mn_{0.8}O_2$, micrometer-sized $Li_{1.2}Nb_{0.2}Mn_{0.6}O_2$ and $Li_{1.3}Nb_{0.3}Mn_{0.4}O_2$ also show improved capacity retention by using HCE (Figure S15, Supporting Information). The use of HCE effectively mitigate the side reaction of oxidized and unstable electrode materials with electrolyte, and thus the dissolution of Mn ions is effectively suppressed, which will be discussed in the following section.

2.4. The Origin of Improvement of Electrode Reversibility for $Li_{1.1}Nb_{0.1}Mn_{0.8}O_2$ with Highly Concentrated Electrolytes

To understand the factors affecting structural reversibility of $Li_{1.1}Nb_{0.1}Mn_{0.8}O_2$ in different electrolytes, in situ XRD study was conducted. The original in situ XRD patterns are plotted in Figure S16 (Supporting Information). Selected 2θ range of 42–45° for 220 diffraction peaks are plotted in **Figure** 5a,b with the

© 2024 The Authors. Advanced Energy Materials published by Wiley-VCH GmbH

16146840, 2024, 23, Downloaded from https://onlinelibrary.wiley.com/doi/10.1002/aenm.202304074 by Yokohama National University, Wiley Online Library on [09/10/2024]. See the Terms and Conditions (https://onlinelibrary.wiley.com/terms-and-conditions) on Wiley Online Library for rules of use; OA articles are governed by the applicable Creative Commons License

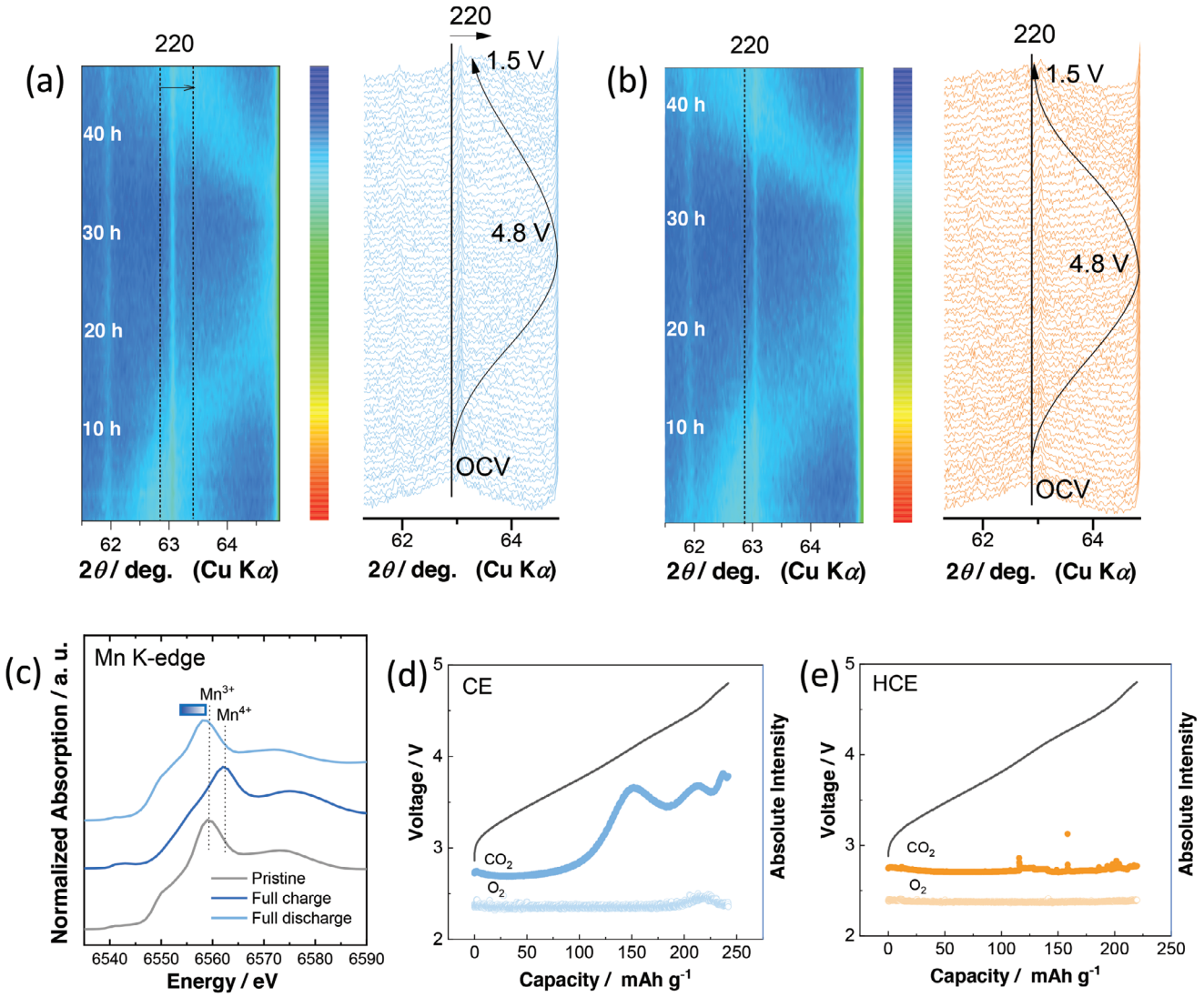

Figure 5. Characterization of nanosized $Li_{1.1-x}Nb_{0.1}Mn_{0.8}O_2$ in different electrolyte solutions: Selected regions of the in situ XRD data and contour maps for $Li_{1.1-x}$ $Nb_{0.1}Mn_{0.8}O_2$ cycled in a) CE and b) HCE, c) ex situ XAS spectra on electrochemical cycles in CE, and the gas evolution measured by OEMS in d) CE and e) HCE. Due to the high volatility of DMC, the evolution of CO_2 and O_2 is compared by absolute intensity for measurement.

corresponding contour maps. Diffraction lines shift to higher diffraction angles on charge, indicating the shrinkage of crystal lattice, and then shift back again after discharge. After fully discharge, the 220 diffraction line for the sample cycled with CE remains at the higher 2θ angle compared with its original position (before charge), indicating irreversible structural change on electrochemical charge/discharge process. This trend is also evidenced by ex situ XRD study (Figure S17, Supporting Information). In contrast, for the case of the sample with HCE, the 220 diffraction line shifts back to the original position, which is also supported by ex situ XRD study (Figure S17b, Supporting Information). Note that the irreversibility of electrochemical reaction is further supported by X-ray absorption spectroscopy (XAS). If the irreversible oxygen loss proceeds on charge, this leads to further reduction of Mn^{3+} on discharge.[46] Changes in Mn K-edge XAS spectra for $Li_{1.1}Nb_{0.1}Mn_{0.8}O_2$ after cycle with CE are shown in Figure 5c. On charge, the energy of XAS spectrum shifts to the higher energy region due to Mn ion oxidation. However, after discharge to 1.5 V, the XAS spectrum is found at a lower energy region in comparison with the pristine electrode. This observation suggests the reduction of Mn ions associated with the oxygen loss on charge. According to our previous study, such irreversible oxygen loss and Mn reduction ions is mitigated for the Li-excess Mn oxides cycled with HCE.[32]

To directly monitor the decomposition of electrolyte on charge, online electrochemical mass spectrometry (OEMS) was also performed (Figure 5d,e). For the sample with CE, CO_2 evolution derived from the oxidative decomposition of carbonate solvents is observed at the voltages higher than 3.7 V. In addition, a small amount of O_2 was detected in the higher voltage regions > 4.6 V. The generation of O_2 gas can be attributed to the destabilization of anionic redox reactions with electrolyte.[47] In contrast, CO_2 and O_2 generation cannot be found in the HCEs at the same condition. The oxidative tolerance of solvent molecules is higher in

© 2024 The Authors. Advanced Energy Materials published by Wiley-VCH GmbH

16146840, 2024, 23, Downloaded from https://onlinelibrary.wiley.com/doi/10.1002/aenm.202304074 by Yokohama National University, Wiley Online Library on [09/10/2024]. See the Terms and Conditions (https://onlinelibrary.wiley.com/terms-and-conditions) on Wiley Online Library for rules of use; OA articles are governed by the applicable Creative Commons License

HCE compared with CE because the most of solvent molecules are coordinated to Li ions in HCE,[48] which may contribute to the suppression of O_2 release from the charged $Li_{1.1-x}Nb_{0.1}Mn_{0.8}O_2$.

The use of oxidatively stable HCE is an effective methodology in suppressing oxygen loss in nanosized $Li_{1.1}Nb_{0.1}Mn_{0.8}O_2$. To further study morphological changes, $Li_{1.1}Nb_{0.1}Mn_{0.8}O_2$ particles cycled in CE and HCE were observed by DF-STEM and BF-STEM (**Figure 6a–c** and Figures S18, S19, Supporting Information). The samples were observed after 10 cycles at a rate of 10 mA g^{-1} in a range of 1.5 – 4.8 V in both electrolytes. From DF-STEM images, a new feature is observed especially for the sample cycled in CE. Many small dark spots are enriched after cycling. Similar dark spots also appear the sample cycled in HCE when compared with the as-prepared sample, but the changes observed in DF-STEM images is much significant for the sample cycled in CE. Recently, a more clear change and the appearance of many dark spots in a DF-STEM image are observed for cycled Li_2MnO_3,[49] which is indicative of the oxygen loss and the formation of nanosized pores inside particles. The enrichment of pores for the sample cycled in CE, is consistent with degradation of electrochemical reversibility and promoted gas generation. Moreover, the oxide surface is covered by electrolyte decomposition products, which are clearly visible for the BF-STEM images for the cycled samples. The oxygen loss is also expected to results in the dissolution of transition metal ions into the electrolyte. Indeed, the purple coloration of electrolyte solution is directly evidenced by ultraviolet-visible absorption spectroscopy (UV–vis) after the storage test of nanosized $Li_{1.1}Nb_{0.1}Mn_{0.8}O_2$ stored in CE at 50 °C for 17 days (Figure 6d). Clear light absorption in a range of >350 nm is clearly observed, which is derived from the Mn ion dissolution into electrolyte. In contrast, after the same storage test in HCE, no coloration is noted, and the dissolution of Mn ions is not evidenced by UV–vis spectroscopy. This fact suggests that Mn ions cannot be dissolved into HCE because of no free solvent molecules in this electrolyte.[31] In addition, PF_6^- ions used for CE are easily decomposed at elevated temperatures, resulting in the formation HF, which causes Mn dissolution into electrolyte.[44,50]

The stabilization mechanisms of nanosized $Li_{1.1}Nb_{0.1}Mn_{0.8}O_2$ with HCE is further studied by X-ray photoelectron spectroscopy (XPS). Electrolyte decomposition products are often deposited on the electrode surface, by which the electrode reversibility is affected.[51,52] Therefore, the surface of $Li_{1.1}Nb_{0.1}Mn_{0.8}O_2$ particles observed by BF-STEM study is analyzed, and XPS spectra of the samples cycled in CE and HCE are summarized in Figure 6e–h and Figure S20 (Supporting Information). The binding energy of XPS spectra was calibrated using a peak of C-H at 284.6 eV in C 1s spectra (Figure S20, Supporting Information), which is mainly derived from acetylene black (AB) in the composite electrodes. Atomic fractions of C-H from AB on the cycled electrodes with both electrolytes are smaller than that on the as-prepared sample (Figure 6i), indicating that AB in the composite electrodes is covered with electrolyte decomposition products. Notably, for the sample cycled in CE, a peak at 287.5 eV is clearly observed in the C 1s spectrum (Figure S20, Supporting Information), which is assigned to C = O containing species originating from the decomposition of carbonate solvents. In the O 1s spectrum, the peak intensity and atomic fraction from lattice oxygen (O^{2-}) are also clearly reduced after cycling in CE (Figure 6g,i). This fact suggests that lattice oxygen is partially oxidized and reacted with the electrolyte solution, leading to CO_2 generation as observed in OEMS spectroscopy (Figure 5d) and accumulation of decomposition products on the surface of oxide particles. The presence of a decomposition product of PF_6^- anion, $Li_xPF_yO_z$,[53] is also noted in the O 1s, F 1s, and P 2p spectra. The P 2p spectrum deconvoluted with spin-orbit split doublets (P $2p_{3/2}$ and P $2p_{1/2}$).[54] These results suggest that the electrode surface after cycling with CE is accumulated by electrolyte decomposition products caused by the side reaction of oxidized $Li_{1.1-x}Nb_{0.1}Mn_{0.8}O_2$.

When the sample is cycled in HCE, a different trend compared with CE is noted. The intensity of a peak originating from C = O is less intensified in both O 1s (Figure 6g) and C 1s (Figure S20, Supporting Information), indicating that the decomposition of carbonate solvents is suppressed compared with CE. This result also supports that HCE has superior oxidative tolerance because of the elimination of free solvents. Although an atomic fraction of O 1s is increased after cycle (Figure 6i), this fact originates from the residue of electrolyte. LiFSA contains S = O species, which is visible in O 1s[44,55] and S 2p[56] spectra. The S 2p spectrum shows doublets split including S $2p_{3/2}$ and S $2p_{1/2}$ core peaks.[56] Peak intensity originating from AB is decreased in C 1s spectra (Figure 6i; Figure S20, Supporting Information), which is indicative of the partial decomposition of HCE on AB surface. Additionally, the enrichment of LiF is evidenced in the F 1s spectrum[57], which is expected to be derived by the decomposition of FSA^- anion. Nevertheless, the atomic fraction of oxide ions from $Li_{1.1}Nb_{0.1}Mn_{0.8}O_2$ is retained (Figure 6g,i) after cycling in HCE, suggesting that the decomposition of HCE on the surface of $Li_{1.1}Nb_{0.1}Mn_{0.8}O_2$ is effectively suppressed.

From these results, it is concluded that the electrode reversibility is significantly improved by the use of the HCE solution with LiFSA. The XPS study reveals that LiFSA and/or DMC is partly decomposed on electrochemical cycles and the decomposition products seems to be accumulated on AB. However, a clear lattice oxygen peak is observed after cycling test, and this fact suggests that the electrolyte decomposition is effectively suppressed on the surface of $Li_{1.1}Nb_{0.1}Mn_{0.8}O_2$ or protected by very thin layers derived from HCE, which is also clearly supported from the characterization results of in situ XRD, UV–vis, STEM, and OEMS spectroscopy, coupled with electrochemical measurements.

3. Conclusion

A binary system of Li_3NbO_4–$LiMnO_2$ is targeted as a potential high energy density positive electrode material, and factors affecting the electrode performance are systematically studied in detail. Although a Li_3NbO_4-rich sample, *e.g*, $Li_{1.3}Nb_{0.3}Mn_{0.4}O_2$, shows a large reversible capacity, ≈300 mA h g^{-1}, capacity retention is unacceptable for practical battery applications. In contrast, a $LiMnO_2$-rich sample, *e.g.*, $Li_{1.1}Nb_{0.1}Mn_{0.8}O_2$, shows a small reversible capacity because of the limitation of percolative ionic conduction, but much improved capacity retention is evidenced. Superior electrode performance of $Li_{1.1}Nb_{0.1}Mn_{0.8}O_2$ is successfully unlocked by the defect engineering and enrichment of grain boundary in oxides. Furthermore, electrode reversibility is significantly improved by the use of HCE, associated with the suppression of electrolyte decomposition and surface stabilization because of the superior tolerance as electrolyte solutions. This finding provides the new possibility to

© 2024 The Authors. Advanced Energy Materials published by Wiley-VCH GmbH

16146840, 2024, 23, Downloaded from https://onlinelibrary.wiley.com/doi/10.1002/aenm.202304074 by Yokohama National University, Wiley Online Library on [09/10/2024]. See the Terms and Conditions (https://onlinelibrary.wiley.com/terms-and-conditions) on Wiley Online Library for rules of use; OA articles are governed by the applicable Creative Commons License

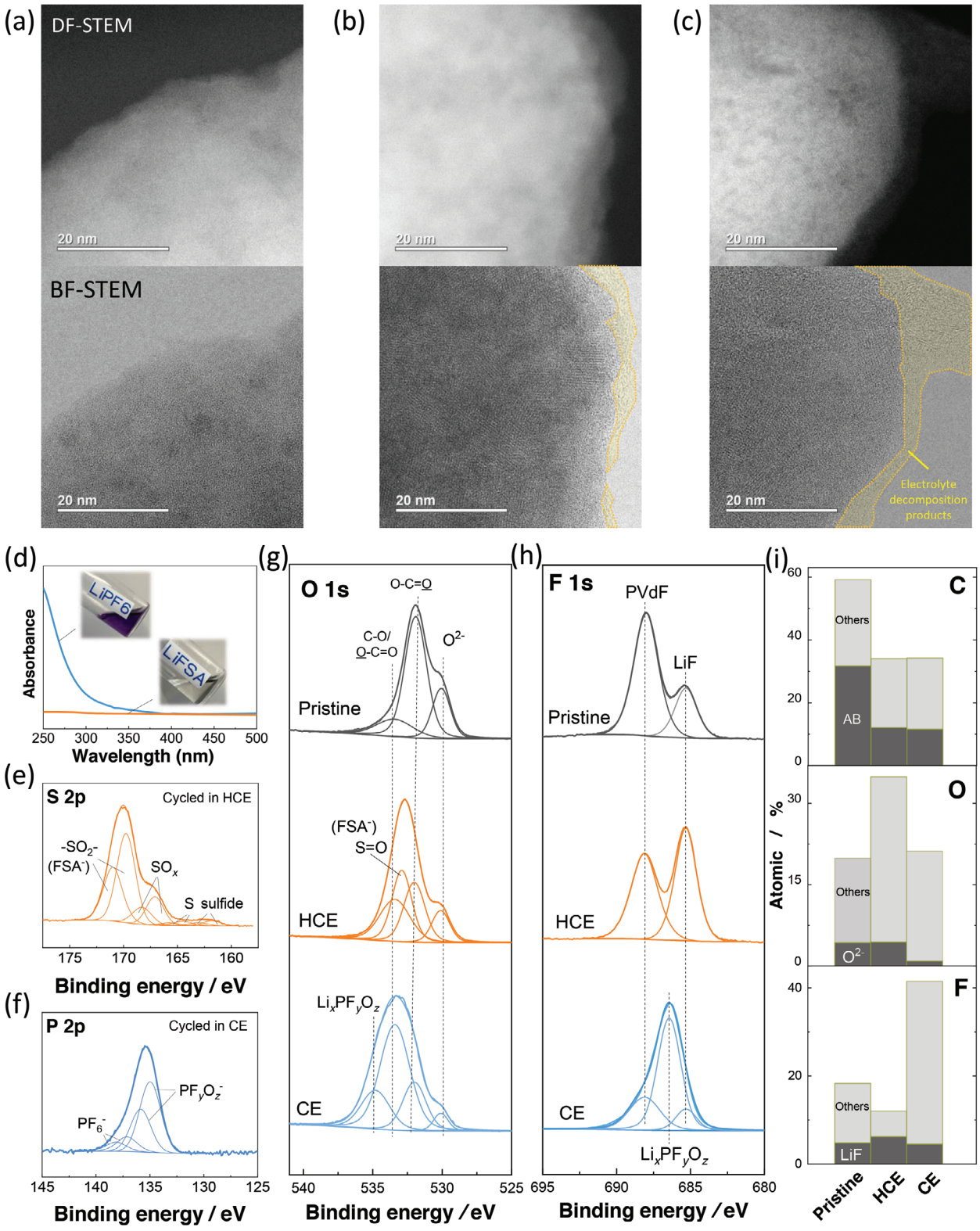

Figure 6. Characterization of nanosized $Li_{1.1-x}Nb_{0.1}Mn_{0.8}O_2$ in different electrolyte solutions: a) DF/BF-STEM images of electrodes cycled in different electrolyte solutions, (a) pristine, b) cycled in HCE, c) cycled in CE. d) Characterization of electrolyte solutions stored with the $Li_{1.1}Nb_{0.1}Mn_{0.8}O_2$ electrode by UV–vis spectroscopy and photo images of the electrolyte after the storage test. XPS spectra of S 2p e), P 2p f), O 1s g), and F 1s h), and i) the atomic fractions of different components, AB, $Li_{1.1}Nb_{0.1}Mn_{0.8}O_2$, and LiF compared with electrolyte decomposition products. For the S 2p and P 2p spectra, spin-orbit split ($2p_{1/2}$ and $2p_{3/2}$) peaks are shown.

© 2024 The Authors. Advanced Energy Materials published by Wiley-VCH GmbH

16146840, 2024, 23, Downloaded from https://onlinelibrary.wiley.com/doi/10.1002/aenm.202304074 by Yokohama National University, Wiley Online Library on [09/10/2024]. See the Terms and Conditions (https://onlinelibrary.wiley.com/terms-and-conditions) on Wiley Online Library for rules of use; OA articles are governed by the applicable Creative Commons License

design high-capacity and high-energy positive electrode materials based on abundant Mn ions, leading to the development advanced high-energy Li ion batteries without non-abundant Ni/Co ions.

4. Experimental Section

Synthesis of Material: Li_3NbO_4-$LiMnO_2$ binary oxides were prepared by a solid-state reaction from Li_2CO_3 (98.5%, Kanto Kagaku), Nb_2O_5 (99.9%, Wako Pure Chemical Industries), and Mn_2O_3. Mn_2O_3 can be produced by heating $MnCO_3$ at 850 °C for 12 h in air. These precursors were mixed by using a planetary ball mill (PULVERISETTE 7; FRITSCH) in a zirconia pot (45 mL) with zirconia balls at 300 rpm for 5 h with ethanol. The mixture was then dried, and pressed into pellets before heating. The pellets were heated at 950 °C for 12 h in an argon atmosphere for $Li_{1.3}Nb_{0.3}Mn_{0.4}O_2$ and $Li_{1.2}Nb_{0.2}Mn_{0.6}O_2$ samples, 1050 °C for 1 h for $Li_{1.1}Nb_{0.1}Mn_{0.8}O_2$ sample. The particle size of $Li_{1.1}Nb_{0.1}Mn_{0.8}O_2$ sample was reduced through mechanical milling in a zirconia pot with zirconia balls at 450 rpm for 3 h, 6 h and 12 h. The mechanical milled powder was taken out from the zirconia pot after every 3 h, and mixed by hand grind using an alumina mortar and pestle to ensure powder uniformity during the milling process. Before making a slurry, all the samples were mixed with acetylene black (HS-100, Denka, active material: acetylene black = 90:10 in wt%) using a planetary ball mill at 300 rpm for 12 h. The obtained carbon composited samples were kept in a glove box before use.

Electrochemistry: Electrode performance of the samples was examined in two-electrode type cells (TJ-AC, Tomcell Japan). The conventional electrolyte used consist of 1.0 mol dm^{-3} $LiPF_6$ dissolved in ethylene carbonate/dimethyl carbonate (EC: DMC = 3:7 by volume) (Kishida Chemical). The highly concentrated electrolyte used consist of lithium bis(fluorosulfonyl)amide (LiFSA) and DMC (5.5 M LiFSA in DMC). The carbon composited positive electrodes consisting of 76.5 wt% active material, 13.5 wt% acetylene black, and 10 wt% poly(vinylidene fluoride), was pasted on an aluminum foil. The electrode slurry was dried under vacuum and further heated at 120 °C in a vacuum for 2 h. A polyolefin microporous membrane was used as a separator for CE, an aramid-coated polyolefin separator was used for HCE.[32] Metallic lithium (Honjo Metal) was used as a negative electrode. Electrochemical impedance measurement was conducted by using a potentiostat equipped with a frequency response analyzer (SP-200, Bio-Logic). All the electrochemical measurements were carried out at room temperature (25 °C on average).

Characterization of Samples: Particle morphology of the samples was observed using a scanning electron microscope (SEM, JCM-6000, JEOL) with an acceleration voltage of 15 kV and scanning transmission electron microscopy (STEM, ARM200F, JEOL) at 200kV. Elemental distributions were measured using STEM with an energy dispersive X-ray spectrometer (EDX, JED-2300T, JEOL) with a resolution of 256×256 pixels. The atomic scale STEM imaging was conducted by HAADF/ABF-STEM using a JEOL JEM-ARM200F instrument with a CEOS CESCOR STEM Cs corrector (spherical aberration corrector) operated at an acceleration voltage of 200 kV. Details of the experimental setup, including specimen preparation, can be found in the literature.[58]

X-ray diffraction (XRD) patterns of the samples were collected using an X-ray diffractometer (D2 PHASER, Bruker) equipped with a one-dimensional X-ray detector using Cu Kα radiation generated at 300 W (30 kV and 10 mA) with a Ni filter. Schematic illustrations of crystal structures of samples were drawn using the program VESTA.[59] In situ XRD patterns were collected using an electrochemical cell equipped with a Be window and X-ray diffractometer (Bruker, D8 Advance) using Cu Kα radiation generated at 1600 W (40 kV and 40 mA) with a Ni filter. The slurry for in-situ measurements was pasted on thin Al foil (5 mm). X-ray photoelectron spectroscopy (XPS, K-Alpha+, Thermo Fisher Scientific) was carried out using monochromatized Al Kα X-ray radiation.

Raman spectra of the samples were collected by using a Raman Microscope (inVia reflex) with a 532 nm laser. The measurement was conducted with a sample holder (LIBcell; Nanophoton) without exposure to air.

Synchrotron XRD data were collected at the beamline BL5S2 in Aichi synchrotron Radiation Center (AichiSR) in Japan. The powders were sealed in capillary samples in Ar atmosphere and measured using the 2D detector (PILATUS 100 K, DECTRIS Ltd.). The wavelength of X-rays was calibrated to be 0.775 Å.

An online electrochemical mass spectrometry (OEMS) was carried out, and the gas evolution was detected during electrochemical measurements. The schematic illustration of the cell for OEMS was described in previous work.[57] The ECCW-Air cell purchased from EL-Cell was used for OEMS measurements. The cell was assembled in an Ar-filled glovebox. An aluminum mesh (20-mesh, 18 mm in diameter, Nilaco) and a Li foil (16 mm in diameter) were used as the working and counter electrodes, respectively. A glass fiber filter (18 mm indiameter, GA-55) wetted with 150 µL of the electrolyte was inserted between the working and counter electrode. Electrochemical measurements were performed using an electrochemical instrument (SP-200, Biologic). The outlet gas from the cell was directly transferred (without column) to a mass spectrometer (GCMS-QP2010 Ultra system, Shimadzu), and electrochemical and MS measurements were performed simultaneously. A carrier gas, He (99.999 vol%), was flowed over the Al mesh electrode at a flow rate of 50 Ml min^{-1}.

Hard XAS spectra were collected with a silicon monochromator in the transmission mode. The intensities of the incident and transmitted X-rays were measured using an ionization chamber at room temperature. Samples for XAS measurements were prepared using the two-electrode cells at a rate of 10 mA g^{-1}. The composite electrodes were rinsed with dimethyl carbonate and sealed in a water-resistant polymer film in the Ar-filled glovebox. Normalization of the XAS spectra was carried out using the program code IFEFFIT.[60] The post-edge background was determined using a cubic spline procedure.

UV–vis spectroscopy was performed on a spectrophotometer (LAMBDA750, PerkinElmer Japan) with wavelength from 250 nm to 500 nm. The two electrodes with the same mass were stored in 800 µL CE or HCE for 17 days, then 100 µL electrolyte was diluted in 3 mL DMC for measurement.

Supporting Information

Supporting Information is available from the Wiley Online Library or from the author.

Acknowledgements

N.Y. acknowledges the partial support from JSPS, Grant-in-Aid for Scientific Research (Grant Numbers 19H05816 and 23K17954). Y.U. also thanks the Grant-in-Aid for Scientific Research (Grant Number 23K13822) from JSPS. This work was partially supported by JST, CREST Grant Number JPMJCR21O6, Japan. This work was in part supported by MEXT Program: Data Creation and Utilization Type Materials Research and Development Project (Grant Number JPMXP1121467561). N.Y. acknowledges the partial support by JST as part of Adopting Sustainable Partnerships for Innovative Research Ecosystem (ASPIRE), Grant Number JPMJAP2313. The synchrotron X-ray absorption work was done under the approval of the Photon Factory Program Advisory Committee (proposal number 2023G028). The authors thank Dr. Yoshinobu Miyazaki and Dr Tomohiro Saito from Sumika Chemical Analysis Service, Ltd for the STEM observation.

Conflict of Interest

The authors declare no conflict of interest.

Data Availability Statement

The data that support the findings of this study are available from the corresponding author upon reasonable request.

© 2024 The Authors. Advanced Energy Materials published by Wiley-VCH GmbH

16146840, 2024, 23, Downloaded from https://onlinelibrary.wiley.com/doi/10.1002/aenm.202304074 by Yokohama National University, Wiley Online Library on [09/10/2024]. See the Terms and Conditions (https://onlinelibrary.wiley.com/terms-and-conditions) on Wiley Online Library for rules of use; OA articles are governed by the applicable Creative Commons License

Keywords

anionic redox, concentrated electrolyte solution, disordered rocksalt, Li-excess oxide, structural defects

Received: November 28, 2023
Revised: March 15, 2024
Published online: April 9, 2024

[1] K. Mizushima, P. C. Jones, P. J. Wiseman, J. B. Goodenough, *Mater. Res. Bull.* **1980**, *15*, 783.
[2] N. Nitta, F. Wu, J. T. Lee, G. Yushin, *Mater. Today* **2015**, *18*, 252.
[3] M. Li, J. Lu, Z. Chen, K. Amine, *Adv. Mater.* **2018**, *30*, 1800561.
[4] T. Ohzuku, Y. Makimura, *Chem. Lett.* **2001**, *30*, 642.
[5] A. Manthiram, J. C. Knight, S.-T. Myung, S.-M. Oh, Y.-K. Sun, *Adv. Energy Mater.* **2016**, *6*, 1501010.
[6] N. Ikeda, I. Konuma, H. B. Rajendra, T. Aida, N. Yabuuchi, *J. Mater. Chem. A* **2021**, *9*, 15963.
[7] D. H. Seo, J. Lee, A. Urban, R. Malik, S. Kang, G. Ceder, *Nat. Chem.* **2016**, *8*, 692.
[8] R. A. House, G. J. Rees, M. A. Pérez-Osorio, J.-J. Marie, E. Boivin, A. W. Robertson, A. Nag, M. Garcia-Fernandez, K.-J. Zhou, P. G. Bruce, *Nat. Energy* **2020**, *5*, 777.
[9] D. Eum, B. Kim, S. J. Kim, H. Park, J. Wu, S. P. Cho, G. Yoon, M. H. Lee, S. K. Jung, W. Yang, W. M. Seong, K. Ku, O. Tamwattana, C.-J. Park, I. Hwang, K. Kang, *Nat. Mater.* **2020**, *19*, 419.
[10] W. E. Gent, K. Lim, Y. Liang, Q. Li, T. Barnes, S. J. Ahn, K. H. Stone, M. McIntire, J. Hong, J. H. Song, Y. Li, A. Mehta, S. Ermon, T. Tyliszczak, D. Kilcoyne, D. Vine, J. H. Park, S. K. Doo, M. F. Toney, W. Yang, D. Prendergast, W. C. Chueh, *Nat. Commun.* **2017**, *8*, 2091.
[11] J. Lee, D. A. Kitchaev, D. H. Kwon, C. W. Lee, J. K. Papp, Y. S. Liu, Z. Lun, R. J. Clement, T. Shi, B. D. McCloskey, J. Guo, M. Balasubramanian, G. ceder, *Nature* **2018**, *556*, 185.
[12] S. Hoshino, A. M. Glushenkov, S. Ichikawa, T. Ozaki, T. Inamasu, N. Yabuuchi, *ACS Energy Lett.* **2017**, *2*, 733.
[13] R. Qi, I. Konuma, B. D. L. Campéon, Y. Kaneda, M. Kondo, N. Yabuuchi, *Chem. Mater.* **2022**, *34*, 1946.
[14] N. Yabuuchi, *Curr. Opin. Electrochem.* **2022**, *34*, 100978.
[15] I. Konuma, D. Goonetilleke, N. Sharma, T. Miyuki, S. Hiroi, K. Ohara, Y. Yamakawa, Y. Morino, H. B. Rajendra, T. Ishigaki, N. Yabuuchi, *Nat. Mater.* **2023**, *22*, 225.
[16] J. Lee, A. Urban, X. Li, S. Dong, G. Hautierand, G. Ceder, *Science* **2014**, *343*, 519.
[17] R. Qi, B. D. L. Campéon, I. Konuma, Y. Sato, Y. Kaneda, M. Kondo, N. Yabuuchi, *Electrochemistry* **2022**, *90*, 037005.
[18] Y. Kobayashi, M. Sawamura, S. Kondo, M. Harada, Y. Noda, M. Nakayama, S. Kobayakawa, W. Zhao, A. Nakao, A. Yasui, H. B. Rajendra, Y. Keisuke, T. Ohta, N. Yabuuchi, *Mater. Today* **2020**, *37*, 43.
[19] J. Lee, C. Wang, R. Malik, Y. Dong, Y. Huang, D. H. Seo, J. Li, *Adv. Energy Mater.* **2021**, *11*, 2100204.
[20] R. J. Clément, Z. Lun, G. Ceder, *Energy Environ. Sci.* **2020**, *13*, 345.
[21] D. Chen, J. Ahn, G. Chen, *ACS Energy Lett.* **2021**, *6*, 1358.
[22] M. Okubo, A. Yamada, *ACS Appl. Mater. Interfaces* **2017**, *9*, 36463.
[23] N. Yabuuchi, M. Nakayama, M. Takeuchi, S. Komaba, Y. Hashimoto, T. Mukai, H. Shiiba, K. Sato, Y. Kobayashi, A. Nakao, M. Yonemura, K. Yamanaka, K. Mitsuhara, T. Ohta, *Nat. Commun.* **2016**, *7*, 13814.
[24] R. Fukuma, M. Harada, W. Zhao, M. Sawamura, Y. Noda, M. Nakayama, M. Goto, D. Kan, Y. Shimakawa, M. Yonemura, N. Ikeda, R. Watanuki, H. L. Andersen, A. M. D'Angelo, N. Sharma, J. Park, H. R. Byon, S. Fukuyama, Z. Han, H. Fukumitsu, M. Schulz-Dobrick, K. Yamanaka, H. Yamagishi, T. Ohta, N. Yabuuchi, *ACS Cent. Sci.* **2022**, *8*, 775.
[25] Y. Zhang, M. Sawamura, M. Harada, Y. Noda, M. Nakayama, M. Goto, D. Kan, Y. Shimakawa, B. D. Louis Campéon, D. Shibata, T. Ohta, N. Yabuuchi, *J. Phys. Chem. C* **2023**, *127*, 2194.
[26] M. Sawamura, S. Kobayakawa, J. Kikkawa, N. Sharma, D. Goonetilleke, A. Rawal, N. Shimada, K. Yamamoto, R. Yamamoto, Y. Zhou, Y. Uchimoto, K. Nakanishi, K. Mitsuhara, K. Ohara, J. Park, H. R. Byon, H. Koga, M. Okoshi, T. Ohta, N. Yabuuchi, *ACS Cent. Sci.* **2020**, *6*, 2326.
[27] Y. Zhang, B. D. L. CampÉOn, N. Yabuuchi, *Electrochemistry* **2023**, *91*, 037004.
[28] A. Kanno, Y. Ugata, I. Ikeuchi, M. Hibino, K. Nakura, Y. Miyaoka, I. Kawamura, D. Shibata, T. Ohta, N. Yabuuchi, *ACS Energy Lett.* **2023**, *8*, 2753.
[29] R. J. Clément, D. Kitchaev, J. Lee, C. Gerbrand, *Chem. Mater.* **2018**, *30*, 6945.
[30] Y. Mahara, N. Nagasako, H. Oka, Y. Kondo, S. Kosaka, H. Nakano, T. Nonaka, Y. Makimura, *ACS Appl. Mater. Interfaces* **2022**, *14*, 24321.
[31] Y. Ugata, N. Yabuuchi, *Trends Chem.* **2023**, *5*, 672.
[32] N. Shimada, Y. Ugata, S. Nishikawa, D. Shibata, T. Ohta, N. Yabuuchi, *Energy Adv.* **2023**, *2*, 508.
[33] D. Chen, W. H. Kan, G. Chen, *Adv. Energy Mater.* **2019**, *9*, 1901255.
[34] H. Ji, A. Urban, D. A. Kitchaev, D. H. Kwon, N. Artrith, C. Ophus, W. Huang, Z. Cai, T. Shi, J. C. Kim, H. Kim, G. Ceder, *Nat. Commun.* **2019**, *10*, 592.
[35] K. Kawai, X.-M. Shi, N. Takenaka, J. Jang, B. M. de Boisse, A. Tsuchimoto, D. Asakura, J. Kikkawa, M. Nakayama, M. Okubo, A. Yamada, *Energy Environ. Sci.* **2022**, *15*, 2591.
[36] Z. Cai, B. Ouyang, H.-M. Hau, T. Chen, R. Giovine, K. P. Koirala, L. Li, H. Ji, Y. Ha, Y. Sun, J. Huang, Y. Chen, V. Wu, W. Yang, C. Wang, R. J. Clément, Z. Lun, G. Ceder, *Nat. Energy* **2024**, *9*, 27.
[37] T. Sato, K. Sato, W. Zhao, Y. Kajiya, N. Yabuuchi, *J. Mater. Chem. A* **2018**, *6*, 13943.
[38] Y. Ugata, C. Motoki, K. Dokko, N. Yabuuchi, *J. Solid. State Electrochem.* **2024**, *28*, 1387.
[39] K. Motohashi, A. Nasu, T. Kimura, C. Hotehama, A. Sakuda, M. Tatsumisago, A. Hayashi, *Electrochemistry* **2022**, *90*, 067009.
[40] P. M. Kibasomba, S. Dhlamini, M. Maaza, C.-P. Liu, M. M. Rashad, D. A. Rayan, B. W. Mwakikunga, *Results Phys.* **2018**, *9*, 628.
[41] G. K. Williamson, W. H. Hall, *Acta Metall.* **1953**, *1*, 22.
[42] V. Biju, N. Sugathan, V. Vrinda, S. L. Salini, *J. Mater. Sci.* **2007**, *43*, 1175.
[43] N. Yabuuchi, M. Sugano, Y. Yamakawa, I. Nakai, K. Sakamoto, H. Muramatsu, S. Komaba, *J. Mater. Chem.* **2011**, *21*, 10035.
[44] J. Wang, Y. Yamada, K. Sodeyama, C. H. Chiang, Y. Tateyama, A. Yamada, *Nat. Commun.* **2016**, *7*, 12032.
[45] S. Chen, J. Zheng, D. Mei, K. S. Han, M. H. Engelhard, W. Zhao, W. Xu, J. Liu, J. G. Zhang, *Adv. Mater.* **2018**, *30*, 1706102.
[46] W.-S. Yoon, C. P. Grey, M. Balasubramanian, X.-Q. Yang, J. McBreen, *Chem. Mater.* **2003**, *15*, 3161.
[47] Z. Lun, B. Ouyang, D. A. Kitchaev, R. J. Clément, J. K. Papp, M. Balasubramanian, Y. Tian, T. Lei, T. Shi, B. D. McCloskey, J. Lee, G. Ceder, *Adv. Energy Mater.* **2018**, *9*, 1802959.
[48] Y. Yamada, J. Wang, S. Ko, E. Watanabe, A. Yamada, *Nat. Energy* **2019**, *4*, 269.
[49] P. Yan, L. Xiao, J. Zheng, Y. Zhou, Y. He, X. Zu, S. X. Mao, J. Xiao, F. Gao, J.-G. Zhang, C.-M. Wang, *Chem. Mater.* **2015**, *27*, 975.
[50] J. Wang, Q. Zheng, M. Fang, S. Ko, Y. Yamada, A. Yamada, *Adv. Sci.* **2021**, *8*, e2101646.
[51] E. Peled, *J. Electrochem. Soc.* **1979**, *126*, 2047.

© 2024 The Authors. Advanced Energy Materials published by Wiley-VCH GmbH

16146840, 2024, 23, Downloaded from https://onlinelibrary.wiley.com/doi/10.1002/aenm.202304074 by Yokohama National University, Wiley Online Library on [09/10/2024]. See the Terms and Conditions (https://onlinelibrary.wiley.com/terms-and-conditions) on Wiley Online Library for rules of use; OA articles are governed by the applicable Creative Commons License

[52] K. Edström, T. Gustafsson, J. O. Thomas, *Electrochim. Acta* **2004**, *50*, 397.
[53] Y.-C. Lu, A. N. Mansour, N. Yabuuchi, Y. Shao-Horn, *Chem. Mater.* **2009**, *21*, 4408.
[54] L. Madec, J. Xia, R. Petibon, K. J. Nelson, J.-P. Sun, I. G. Hill, J. R. Dahn, *J. Phys. Chem. C* **2014**, *118*, 29608.
[55] J. Alvarado, M. A. Schroeder, M. Zhang, O. Borodin, E. Gobrogge, M. Olguin, M. S. Ding, M. Gobet, S. Greenbaum, Y. S. Meng, K. Xu, *Mater. Today* **2018**, *21*, 341.
[56] Y. Yamada, K. Furukawa, K. Sodeyama, K. Kikuchi, M. Yaegashi, Y. Tateyama, A. Yamada, *J. Am. Chem. Soc.* **2014**, *136*, 5039.
[57] Y. Ugata, R. Tatara, T. Mandai, K. Ueno, M. Watanabe, K. Dokko, *ACS Appl. Energy Mater.* **2021**, *4*, 1851.
[58] T. Masese, Y. Miyazaki, G. Mbiti Kanyolo, T. Takahashi, M. Ito, H. Senoh, T. Saito, *ACS Appl. Nano Mater.* **2021**, *4*, 279.
[59] K. Momma, F. Izumi, *J. Appl. Crystallogr.* **2011**, *44*, 1272.
[60] M. Newville, *J. Synchrotron Rad.* **2001**, *8*, 322.

© 2024 The Authors. Advanced Energy Materials published by Wiley-VCH GmbH

16146840, 2024, 23, Downloaded from https://onlinelibrary.wiley.com/doi/10.1002/aenm.202304074 by Yokohama National University, Wiley Online Library on [09/10/2024]. See the Terms and Conditions (https://onlinelibrary.wiley.com/terms-and-conditions) on Wiley Online Library for rules of use; OA articles are governed by the applicable Creative Commons License